Investigation of turbulent superstructures in Rayleigh-Bénard convection by Lagrangian particle tracking of fluorescent microspheres

Stephan Weiss[1], Daniel Schanz[1], Ahmed Oguzhan Erdogdu[1], Andreas Schröder[1,2], Johannes Bosbach[1]

1: Department of Experimental Methods, Institute of Aerodynamics and Flow Technology,
German Aerospace Center (DLR), Göttingen, Germany
2: Brandenburgisch Technische Universität (BTU) Cottbus-Senftenberg, Germany

*Corresponding author: stephan.weiss@dlr.de

Keywords: Lagrangian particle tracking, Turbulence, Thermal convection, Shake-The-Box, Rayleigh-Bénard convection, Turbulent superstructures.

ABSTRACT

We present spatially and temporally resolved velocity measurements of turbulent Rayleigh-Bénard convection (RBC) in a fluid sample of square horizontal cross section with length $L = 320\,\mathrm{mm}$ and height $H = 20\,\mathrm{mm}$, resulting in an aspect ratio of $\Gamma = H/L = 16$. The working fluid was water with a Prandtl number of *Pr*=7 and the Rayleigh-number was set to $Ra = 1.1 \times 10^6$. We seeded the flow with fluorescent polyethylene microspheres that were photographed at a rate of 19 Hz by six cameras. From the images the particle position and their velocity was calculated via the "Shake-The-Box" (STB) Lagrangian particle tracking algorithm. With this approach, we could simultaneously track more than 300,000 particles and hence study the resulting turbulent structures in the Eulerian and Lagrangian frames.

1. Introduction

Thermal convection describes the fluid flow driven by a thermal gradient. It plays a major role as an efficient heat transfer mechanism in nature and industry and is the driving force behind large scale flow systems in many geo- and astrophysical settings. Convection is usually studied numerically and experimentally in an idealised model system, where a horizontal fluid layer of height H is confined by a warm plate from below and a cold plate from above. This system is known as Rayleigh-Bénard convection (RBC) and has been studied for over a century (see e.g., Bénard (1900); Rayleigh (1916); Kadanoff (2001); Ahlers et al. (2009)). When the temperature difference $\Delta = T_b - T_t$ between the bottom (T_b) and the top (T_t) is sufficiently small, relevant physical properties of the fluid can be assumed to be constant and the system is only governed by two control parameters. These are

$$Ra = \frac{g\alpha\Delta H^3}{\nu\kappa} \text{ (the Rayleigh number) and } \quad Pr = \frac{\nu}{\kappa} \quad \text{(the Prandtl number).} \tag{1}$$

Here, g, α, ν and κ denote the gravitational acceleration, the isobaric thermal expansion coefficient, the kinematic viscosity, and the thermal diffusivity. The Rayleigh number indicates the ratio between the driving buoyancy and the damping mechanisms, i.e., momentum and thermal diffusion, whereas *Pr* is the ratio of the latter two. Next to *Ra* and *Pr* also the geometrical constrains plays a role. For a given geometry, this is expressed by the aspect ratio between the lateral dimension L and the height $\Gamma = L/H$.

For small *Ra*, the flow is laminar and RBC serves as a model system to study pattern formation (Bodenschatz et al., 2000). In fact, for a laterally extended fluid layer ($\Gamma \gg 1$), when the effect of the lateral boundaries is small, convection sets in at a critical value $Ra_c = 1708$ in the form of stationary periodic rolls with a wave number of $k_c = 3.117/H$ (wave length of $\lambda_c = 2\pi/k_c \approx 2H$). With increasing thermal driving, the initially steady rolls become dynamic, chaotic and finally, at sufficiently large *Ra*, the flow turns turbulent. Most studies focussing on this regime aim to understand how and how much thermal energy is transported from the bottom to the top as a function of the applied temperature difference (Ahlers et al., 2009).

In order to increase the thermal driving and also for practical reasons, turbulent convection is predominantly studied in boxes or cylinders of a lateral extent similar to their height $\Gamma \approx 1$. In these cases, the flow is dominated by a large scale convection roll, in which warm fluid rises on one side and cold fluid sinks at the opposite side. As typical for turbulent flows, the kinetic energy of the large scale structure is transferred into smaller eddies and eventually dissipated into heat in the smallest eddies. Warm (cold) fluid volumes, so called *plumes*, rise (sink) from the bottom (top) and carry potential energy, which is converted into kinetic energy of the large roll.

Many different aspects of such small aspect ratio systems have been investigated in the past (see e.g., Ahlers et al. (2009); Lohse & Xia (2010); Chillà & Schumacher (2012)). However, only recently have researchers started to focus on the largest scales and to investigate how the flow structure changes when it is given more space in lateral direction (see e.g., Ambrish Pandey & Schumacher (2018); Stevens et al. (2018)). It was observed that in these cases, structure is hidden in the turbulent flow that resembles the convection rolls close to convection onset. This structure becomes visible in particular in the vertical velocity and the temperature field upon averaging over sufficiently long time scales and are called *turbulent superstructures* (TSS). Albeit the turbulent superstructures are less coherent and less ordered than their laminar counter part at small *Ra*, they have a well defined wave length as well. Simulations by Ambrish Pandey & Schumacher (2018) suggest that the wave length increases with *Ra* from $\lambda \approx 2H$ close to convection onset to $\lambda \approx 6H$ for the fully turbulent regime. However, the exact value depends on the aspect ratio Γ as well and can only be reached in sufficiently wide domains, i.e., large Γ (Stevens et al., 2018). The dynamics, shape or even the size of the TSS are so far not understood. Only recently have attempts been made to model the increase in wave length by adding a noise term representing, the vigorous turbulent fluctuations, to the Swift-Hohenberg-model (Ibbeken et al., 2019).

The energy spectrum of vertical velocity exhibits a broad maximum at the wavelength of the superstructures with a large decaying turbulent tail for larger wave numbers. However, if one considers

the power spectrum of the temperature field or the vertical heat flux, a distinct peak is observed at the largest scales that is clearly separated from a rather broad peak due to the turbulent small scale fluctuations (Hartlep et al., 2003; Krug et al., 2020). We also note in this context that similar TSS also occur in Taylor-Couette flow, where the laminar patterns at weak driving become turbulent but are still observable upon averaging under strong driving (Huisman et al., 2014).

Investigating such large aspect ratio systems is important to better understand many natural systems such as the Earth's atmosphere where the height of which is rather small compared to its lateral dimensions. However, they are difficult to address in direct numerical simulations, as the performance of computers is limited and even nowadays still insufficient to resolve both the largest and the smallest relevant length scales simultaneously over a sufficient time span. While in experiments, it is usually easier to make long time measurements, it is rather complicated to measure the entire velocity field with sufficiently high resolution. So far, only very few time-resolved volumetric velocity measurements have been conducted in RBC (Bosbach et al., 2021; Paolillo et al., 2021), predominantly in cells of small aspect ratios. Planar (long-term) measurements in high-aspect ratio samples were already successfully conducted by Moller et al. (2021), who have seeded their flow with thermochromic liquid crystal particles. The particles temperature was determined from their color and velocities were measured via stereo-particle image velocimetry. The successful measurement of both quantities allowed to also determine the vertical heat flux along two horizontal cross sections of the cell (at midheight and close to the top plate). In this experiment the authors could follow the dynamics of the turbulent superstructures over more than 3000 free-fall times ($t_f = \sqrt{H/g\alpha\Delta}$).

In this paper here, we present results from volumetric long-term particle tracking measurements in a rectangular RBC cell of aspect ratio $\Gamma = 16$. From these measurements, we calculate the three-dimensional morphology of the turbulent large-scale structures, as well as their temporal evolution and dynamics.

2. Experimental setup

Our experimental setup is sketched in fig. 1(a). We used distilled water as the working fluid to which sodium chloride was added (0.25 per cent in mass) in order to match the density of the seeding particles. The water was confined in a rectangular Rayleigh-Bénard cell with a square horizontal cross-section of side length $L = 320\,\mathrm{mm}$. The cell height was given by the sidewall that was used and hence could easily be adapted. Here, we present results from a cell with height of $H = 20\,\mathrm{mm}$ corresponding to an aspect ratio of $\Gamma = L/H = 16$. The bottom plate was made out of aluminum and was electrically heated via an carbon fiber fabric glued at its bottom and thermally insulated from below. Four resistance temperature detectors in the bottom plate have been used to measure the temperature and a PID feedback loop was used for regulating the heat input into the bottom plate to keep T_b constant.

The top plate was a 0.5 mm thin borosilicate glass plate for providing optical access. It was cooled

by pumping cooling water at a well defined temperature through a cavity above its top. The temperature of the cooling water was regulated by a chiller and is kept constant to within ± 10 mK. The temperature at the top (T_t) and bottom (T_b) plates were regulated so that their mean $T_m = (T_b + T_t)/2$ stays constant at $T_m = 20.0 \pm 0.01$ °C, resulting in a $Pr = 7.0$. The applied temperature difference between the bottom and the top plate could easily be varied but was set for the experiment presented here to $\Delta = 10$ K resulting in $Ra = 1.1 \times 10^6$.

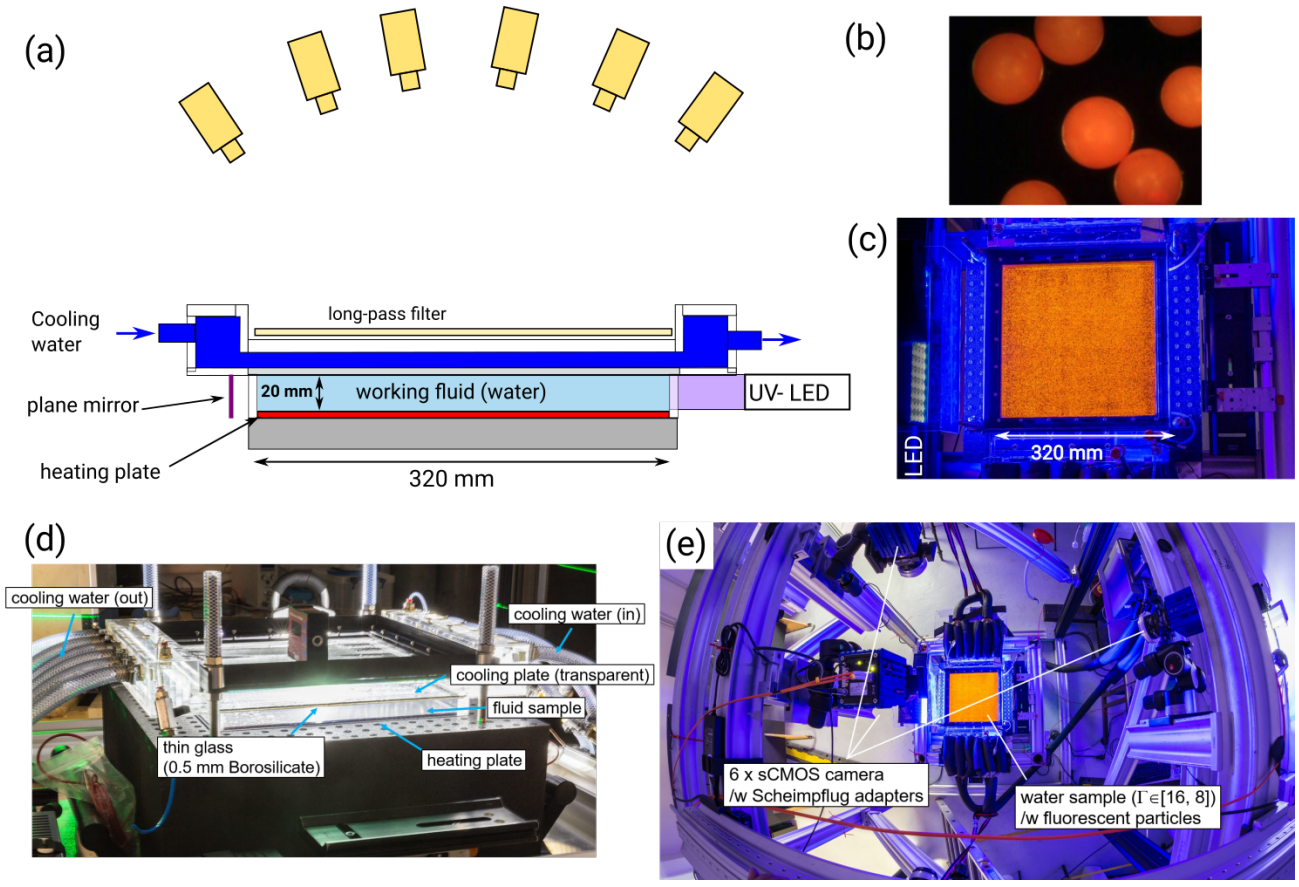

Figure 1. Experimental setup. (a) Schematic of the experimental setup. (b) Image of the $\approx 50\mu$m large fluorescent polyethylene microsphere that were used for seeding the flow. (c) Photo of the high aspect ratio convection cell with a quadratic horizontal cross-section from the top. When illuminated with UV light from the side, the microspheres emit orange light with a maximum at a wavelength of about 600 nm. (d) Side view of the rectangular convection cell. (e) Top view of the entire setup showing the arrangement of the cameras. This photo was captured with a fisheye lens and hence is distorted at its sides (photographic work by J. Agocs).

For flow visualisation, we seeded the fluid with fluorescent polyethylene microspheres (d $\approx 45 - 53\,\mu$m) as tracer particles, which were illuminated by two pulsed UV-LED arrays (LaVision) from the sides through the transparent sidewall. The illumination was further enhanced by placing flat mirrors on the opposites sidewalls (see also fig. 2). The particles had a density of $\rho = 1.00 \times 10^3$kg/m^3, similar to the density of the working fluid and hence can be considered neutrally buoyant. The particles absorbed light in the near UV range and emit at wavelength longer than 580 nm. Hence we filtered out scattered light from the LEDs by placing a long-pass filter (3 mm thick Perspex "orange", 550 nm) atop the flow distributor of the cooling liquid. This has significantly in-

creased the image quality since the convection cell is rather thin and reflections from the boundaries were unavoidable.

We have used six scientific CMOS cameras (2560 $\times$ 2160 px) to image the particles from different angles. The four most outer cameras were equipped with 60 mm lenses (Zeiss Makro-Planar 2.8/60) and the two inner cameras with 50 mm lenses (Zeiss Planar T* 1.4/50), which were mounted on the cameras via Scheimpflug-adapters to account for the oblique viewing angles.

The imaging system was calibrated by positioning a two layer calibration grid at vertical distances $z = 0$ and H from the bottom plate in place of the actual convection cell in order to mimic the optical transmission of light from the apparatus as closely as possible (fig. 2). In addition, we also performed a volumetric self-calibration (Wieneke, 2008) and a calibration of the particle imaging (Optical Transfer Function, (Schanz et al., 2012)) during an actual measurements with low seeding density. In this way we could map the real world coordinate system to the camera image with sub-pixel precision.

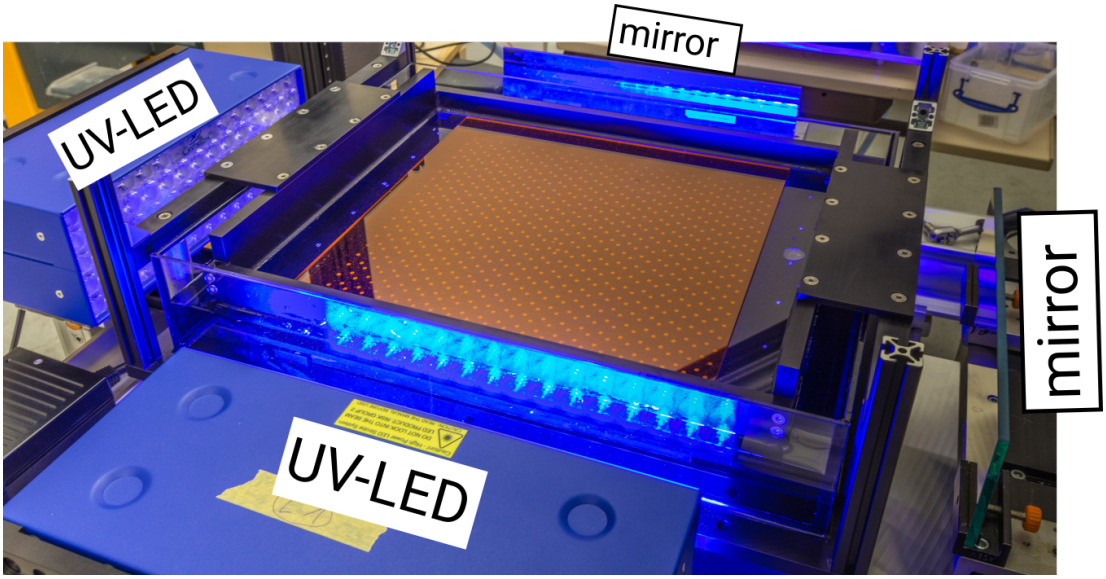

Figure 2. Cell with calibration grid.

From the camera snapshots, the position of the microspheres as well as their velocity and acceleration as function of time was calculated using the *Shake-The-Box* algorithm (Schanz et al., 2013, 2016). Specifically, the DLR implementation of the Variable-Timestep-STB processing (Schanz et al., 2021) was applied to the images that showed particle peaks in a density of approx. $N_I = 0.06$ particles-per-pixel (ppp). This allowed following over 300,000 particles for an extended time, most of them for thousands of time-steps. The gained raw particle positions were filtered using the 'TrackFit'-approach (Gesemann et al., 2016), with a crossover frequency calibrated via the position spectrum of the unfiltered tracks. This procedure also allows to quantify the average position accuracy, being approx. 7 μm for the x- and y-corrdinate and 20 μm for the z-coordinate in case of the raw tracks. The filtering process roughly halves the given values.

We used the Lagrangian particle field to further calculate highly resolved Eulerian velocity fields

using FlowFit (Gesemann et al., 2016). FlowFit returns a continuous three-dimensional velocity field by minimizing a cost function comprised of the residual of the particle positions and the velocity field taking the incompressible Navier-Stokes equations into consideration. In the case presented here, we calculated the velocity on a grid with a grid spacing of roughly one Kolmogorov length ($\eta \approx 1\,\mathrm{mm}$) in all three directions. On average, the velocity and acceleration of 0.14 particles were used to calculate the velocity in one unit cell of the grid. The regularization via the governing equations increases the reconstructed spatial resolution beyond the sampling by the particles.

During an experimental run, the temperature of the cooling bath and the bottom plate was set to their desired temperatures. After that, the tracer particles were dispersed by moving a thin rod magnetically close to the bottom plate. The flow was then given sufficient time so that the introduced fluid motion could fully decay and the resulting flow was purely driven by thermal gradients. We took snapshots with a frequency of 19 hz which are roughly 18 images per Kolmogorov time $t_\eta = \sqrt{\nu/\varepsilon}$, with ε representing the average energy dissipation rate. In total we took 38000 snapshots with each camera, covering a time span of 2000 t_f.

3. Results

Our main focus of interest are the morphology and the dynamics of the largest structures in the flow with the slowest dynamics , i.e., the *turbulent superstructures*. Figure 3(a and b) show horizontal and vertical cross-sections of snapshots of the tracked particles. In both figures, all particles are shown that were tracked and are located in a thin slice that is 2 mm (a) or 4 mm (b) wide at a given time. The color of the data points corresponds to their vertical velocity in units of the free-fall velocity $u_f = \sqrt{g\alpha\Delta H}$ (i.e., a hypothetical velocity that is reached by a fluid parcel after a distance H under constant acceleration $g\alpha\Delta/2$). In this representation, areas where warm fluid rises (red) and where cold fluid sinks (blue) can clearly be distinguished. In particular in fig. 3(a), the large scale flow patterns are already visible, even though the distribution of red and blue dots is still chaotic and the coherence of the structure is lost over rather short distances. In the vertical cross-section (fig. 3b) on the other hand, we see that warm (red) upflow and cold (blue) downflow occurs in rather narrow regions that are very coherent in the vertical direction. We note that coherent regions of upflow or downflow are not equally spaced, since the large scale structures are aligned with different angles to the vertical plane considered here.

We also show in fig. 3(c) vertical profiles of the averaged horizontal ($\langle u^2 + v^2 \rangle$) and vertical ($\langle w^2 \rangle$) turbulent kinetic energy (TKE). For this, data were averaged over time and the horizontal coordinate and the result is normalised with u_f. The shape of these profiles are typical and as expected for Rayleigh-Bénard convection. The maxima of the horizontal TKE are located rather close to the top and bottom, which is a result of the largest convection pattern that span the entire vertical extent of the cell. Due to these structures, shear boundary layers occur close to the top and bottom plate, which can be considered laminar since the shear stress therein is too small to render them turbulent (Grossmann & Lohse, 2000; Ahlers et al., 2009). However, due to hot and cold plumes

that detach from the bottom and top plates, the boundary layers are constantly perturbed by these frequent ejections of highly buoyant fluid. The vertical TKE (red) has a maximum at midheight, which again is in congruence with the observation of the large-scale structures (see also fig. 4). The largest accelerations occur near the top and bottom plates, where temperature gradients an therefore also buoyancy is large. Subsequently the largest vertical velocity have to occur in the vertical center before pressure gradients close to the opposite plate decelerates the fluid.

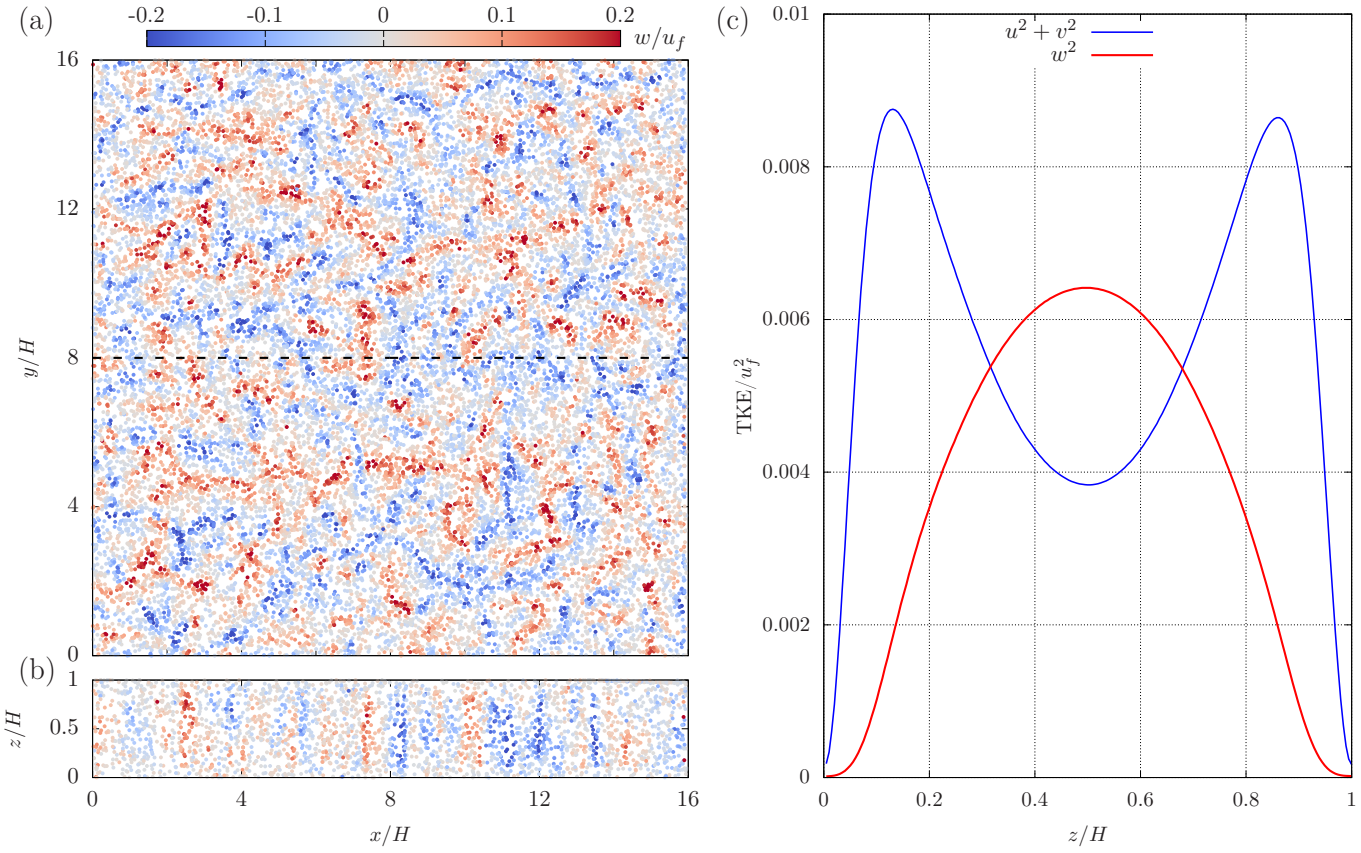

Figure 3. (a and b): Horizontal and vertical cross-sections of snapshots of the tracked particles. The color of each point denotes the vertical velocity in units of u_f, i.e., red for the rising particles, and blue for sinking particles. (a) shows the particles at midheight ($z = 0.5 \pm 0.05$ H). (b) shows the particle at y=8H, i.e., around the horizontal dashed line in (a). Note that the ratio of the x- and y-axis in (b) is not preserved for better visibility. (c): Vertical profiles of the space and time-averaged horizontal and vertical turbulent kinetic energy as a function of the vertical distance from the bottom plate.

Large scale structures in turbulent systems are usually affiliated with longer time scales, whereas small scale fluctuations occur on short time scales. As we are mainly interested in characterising the largest flow structures, i.e., the TSS , we average the instantaneous velocity fields over various time intervals in the following. For best observing the turbulent superstructures this time interval should be long enough, so that small scale fluctuations are averaged out, but not so long that the intensity of the interesting pattern is reduced. This is crucial, since also the largest structures are dynamic and both move and deform rather randomly in time. Therefore, in an ideal and perfectly

symmetric system, no mean flow is expected to occur after averaging over sufficiently long time intervals.

We show in fig. 4 horizontal slices of the vertical velocity field at midheight (left column) and close to the bottom plate (right column). Note that velocity close to the top plate is not shown but looks very similar to the velocity at the bottom, but color-inverted due to the up-down symmetry of the system. Figure 4(a) displays snapshots, whereas fig. 4(b and c) present velocity fields that were averaged over 25 (b) and 50 (c) free-fall times.

There are clear qualitative differences between the velocity fields at midheight and close to the bottom, in particular in the instantaneaous snapshots (fig. 4a). There, one sees that the blue (sinking) and red (rising) structures are rather symmetric in shape and distribution at midheight (left), whereas at the bottom, a network of red thin line-like structures exists with patches of blue areas enclosed by them. These line structures are formed by rising warm plumes and the interaction between them. It seems that the dominant length scale at the bottom is determined by the spacing of these *line plumes*. Larger patterns are not visible. The snapshot of the velocity field at midheight looks qualitatively different from the cross-section close to the bottom plate. Most importantly, the network of line-plumes is not visible at midheight due to viscous diffusion and the red (upwelling) and blue (downwelling) areas are similar in size and structure. However, also at midheight, the instantaneous velocity field looks rather chaotic and a large scale structure is only hardly visible.

Upon averaging over 25 or even 50 free-fall times (fig. 4b and c) long-living large scale structures become dominant in the flow fields, consisting of a complex network of cellular and roll-like structures, which we refer to as TSS. The averaged flow field at the bottom and the midheight looks more similar and the TSS are visible in both. These structures are sharp only when averaging over limited periods as the TSS themselves move and change with time. Especially the arrangement and abundance of the cellular and roll-like structures is subject to temporal evolution.

We now want to deduce the relationship between typical time scales of the bespoken structure and their size. For this we decompose the spatiotemporal dataset of the vertical velocity in its most important contribution via *proper orthogonal decomposition* (POD) (see e.g.,(Lumley, 1967; Berkooz et al., 1993)). This method represents the temporal evolution of an m-dimensional signal $\mathbf{u(t)} = [\mathbf{u_1(t)}, \mathbf{u_2(t)}, \ldots, \mathbf{u_m(t)}]$ as a linear combination of the most important fundamental modes ($[\boldsymbol{\phi_1}, \boldsymbol{\phi_2}, \ldots, \boldsymbol{\phi_n}]$):

$$\begin{bmatrix} \mathbf{u(t_1)} \\ \mathbf{u(t_2)} \\ \vdots \\ \mathbf{u(t_n)} \end{bmatrix} = \begin{bmatrix} A_{11} & A_{12} & \ldots & A_{1m} \\ A_{21} & A_{22} & \ldots & A_{2m} \\ \vdots & \vdots & \vdots & \vdots \\ A_{n1} & A_{n2} & \ldots & A_{nm} \end{bmatrix} [\boldsymbol{\phi_1}, \boldsymbol{\phi_2}, \ldots, \boldsymbol{\phi_n}]. \tag{2}$$

Here, the A_{ik} are the k-th time coefficient for the i-the mode. Note that modes are ordered according to their contribution to the total turbulent kinetic energy (the eigenvalues of the covariance matrix), so that mode ϕ_1 contributes most to the signal. Of course, the individual POD modes (ϕ_i) strongly depend on the time interval considered.

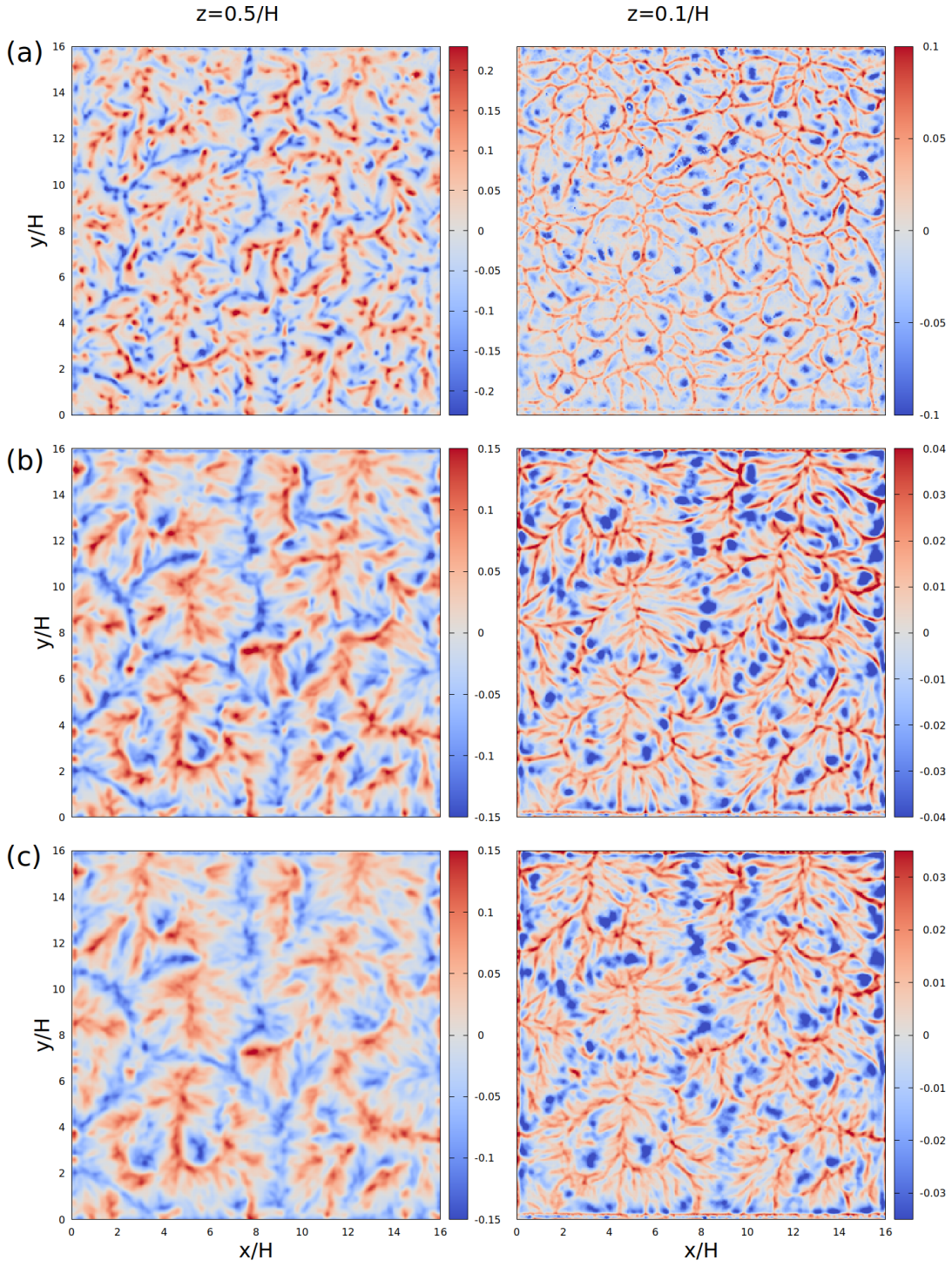

Figure 4. Eulerian field of the vertical velocity component (in units of u_f) at midheight (left column) and close to the bottom plate (right column). Row (a) shows snapshots, (b) an average over 25 free-fall times and (c) an average over 50 free-fall times.

This is neatly demonstrated in fig. 5, where isosurfaces are shown of the first POD mode calculated from the three-dimensional vertical velocity over a time period of $\approx 5t_f$ (fig. 5a and c) and over $\approx 50t_f$ (fig. 5b and d). Shown are isosurfaces surrounding volumes with a vertical velocity larger

than 0.025 u_f (red) and smaller than -0.025 u_f (blue).

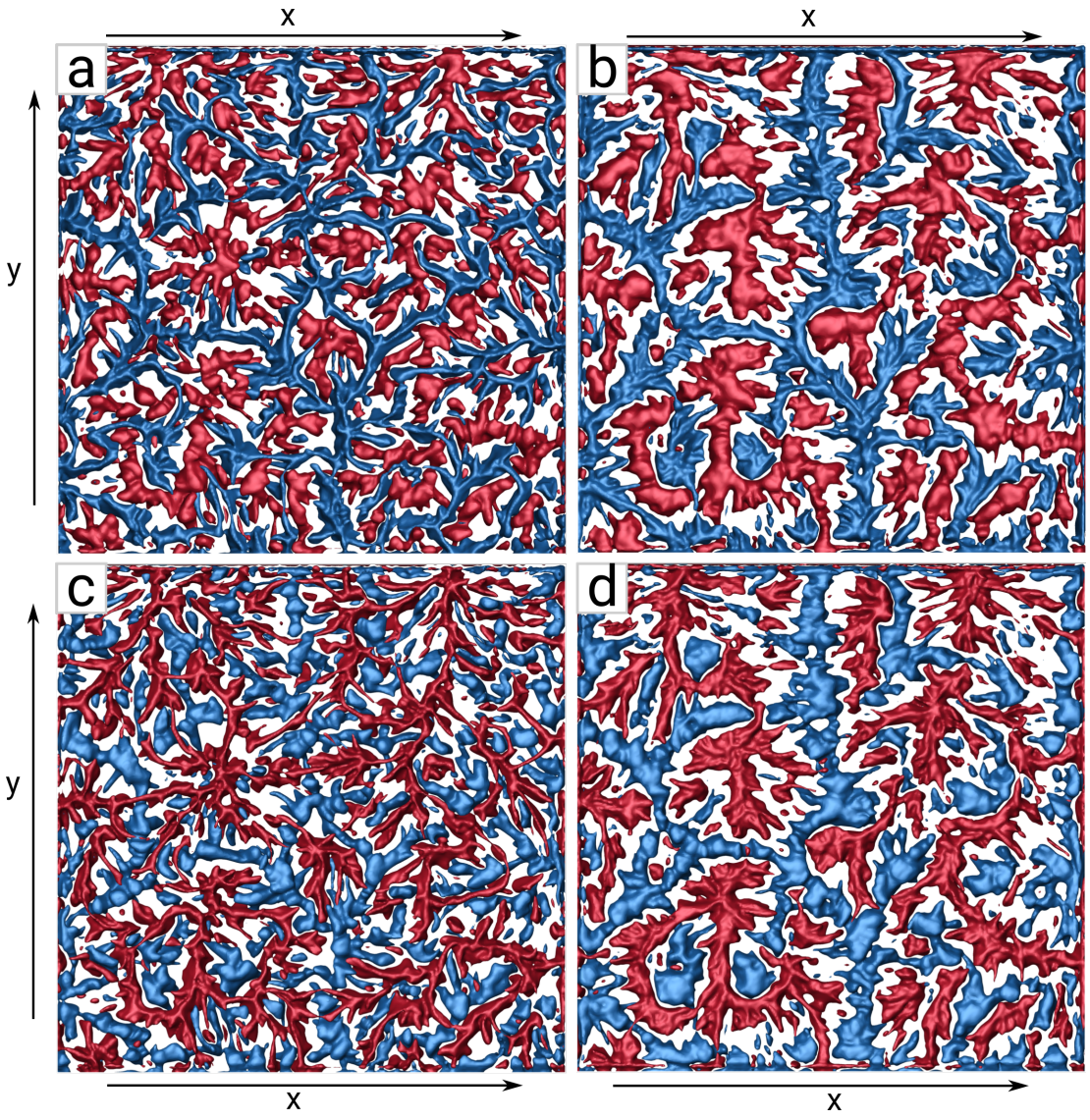

Figure 5. Isosurfaces of the 1st POD mode at $-0.025\,u_f$ (blue) and $0.025\,u_f$ (red) that was calculated from the evolution of the vertical velocity field over a time interval of $\approx 5t_f$ (a and c) and $\approx 50t_f$ (b and d). (a and b): View from the top. (c and d): View from the bottom, with an inverted x-direction to better compare with the top view.

The blue volumes are rather thin at the top (fig. 5a and b) and widen towards the bottom (fig. 5c and d), while the red updraft areas are wide at the top and narrow at the bottom. This up-down symmetry is due to the qualitative difference between regions where plumes form and detach from the boundary layer (ejection regions) and regions where they reach the opposite plate (plume impacting regions).

Similar to fig. 4 we clearly see in fig. 5 that the dominant structures become larger and more pronounced while small scale pattern disappear when longer time scales are considered (comparing fig. 5 a and b). In fact the 1st POD mode is very similar to a simple averaged velocity field. However, in contrast to a simple average, by performing a POD the small scale structures are not lost,

but are rather available in the higher order modes. Therefore, we want to look now at these higher order modes, and see over which time scales they exist.

To compare different POD modes, we show in fig. 6 horizontal cross-sections of the six most dominant modes. In fact fig. 6 shows POD modes performed on horizontal cross-sections of the vertical velocity at midheight, calculated over $\approx 50t_f$. The first mode, again, is rather similar to the averaged velocity field shown in fig. 4(c). The small scale fluctuations that occur on short time scales, which were averaged out in fig. 4(c) are visible in fig. 6(b-f). There, one can clearly see how the structures become smaller with increasing mode number.

We further observe that the structures become more isotropic with increasing mode number. The dominant patterns in fig. 6(a) consist of rather long extended ridges, denoting the large scale convection rolls. Also, the structures visible in the 2nd (b) and 3rd mode (c), albeit smaller, show elongated red and blue patches, which are still somehow aligned over short distances. However, the alignment gets more and more lost for higher modes and also the structures themselves become more and more round. This demonstrates neatly how in turbulence information from the largest scales are lost when energy is transferred to smaller scales, at which the flow becomes rather isotropic.

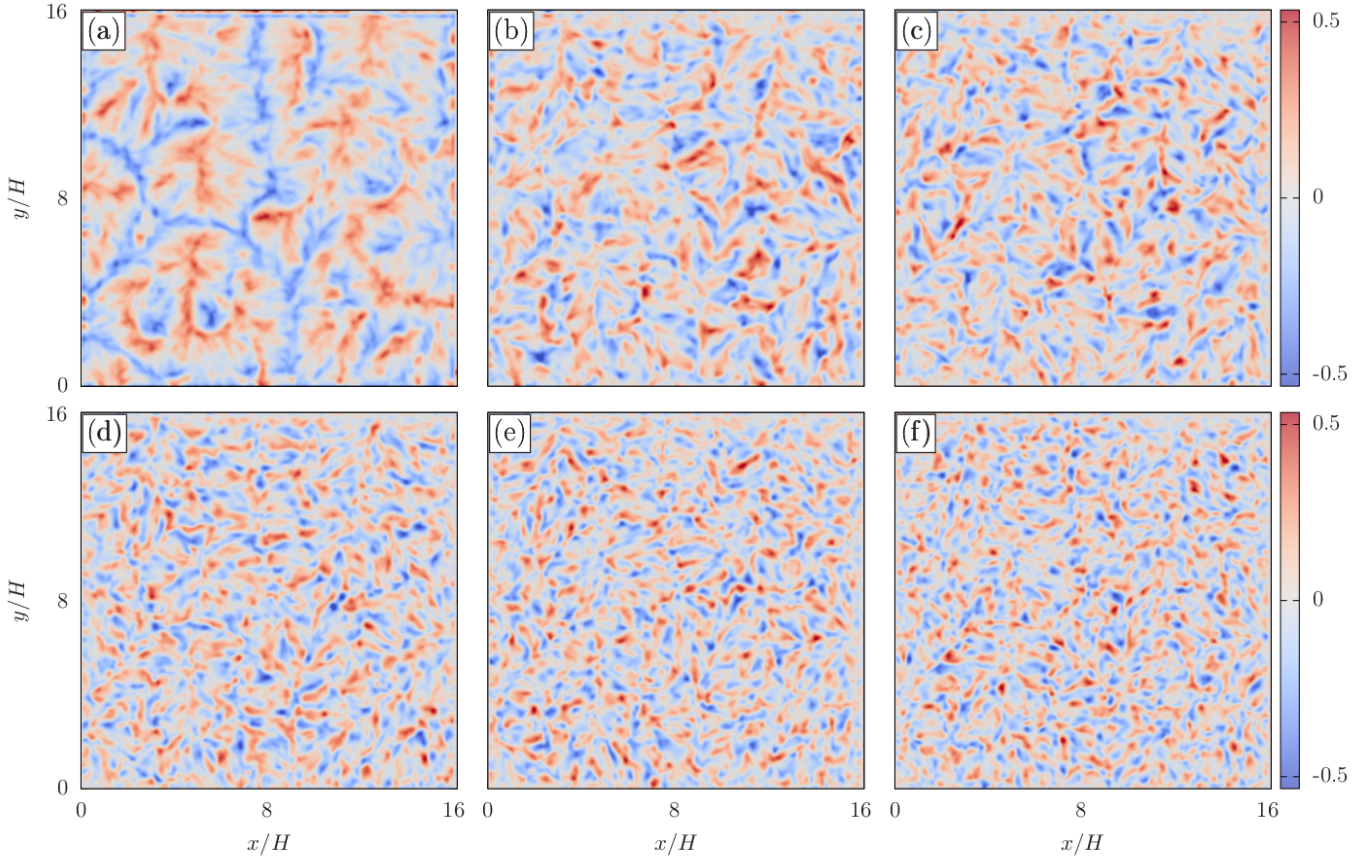

Figure 6. First 6 POD modes of the 2d-vertical velocity field at midheight, calculated over $\approx 50t_f$. The color code mark POD value in units of u_f.

Of course, just calculating the individual POD modes is only helpful if we also consider their relative contribution to the flow, i.e., their eigenvalues. The eigenvalue spectrum of all modes is shown in fig. 7(a), plotted on a semi-log plot. The first eigenvalue is significantly larger than the second eigenvalue by a factor of 1.5, suggesting that indeed the TSS in Rayleigh-Bénard convection are not just merely the largest structures in an otherwise continuous spectrum. The higher modes decay, initially exponentially with their mode number, but the decay slows down at around the 45th eigenvalue (black vertical line in fig. 7a). Even larger modes have a rather flat spatial Fourier spectrum which represents random white noise rather than information about the flow.

We have seen already in fig. 6 that the visible structure in each mode becomes smaller with increasing mode number. In order to quantify the size of the pattern in each mode, we calculated the 2-dimensional spatial Fourier-spectrum which we then average over the azimuthal direction, in order to get a wave number spectrum for each mode. The result is shown in fig. 7(b). The two down-pointing red arrows mark wave numbers $k = 3.117$, i.e., the critical wave number for the convection rolls at their onset for an infinite system (Bodenschatz et al., 2000), and $k = 1$, which is the wave number that is expected for the larges structures at large *Ra* in spatially extended systems (Stevens et al., 2018).

In this figure, the maximum of the power spectra for mode 1 is rather close to $k = 1$ as has been observed in numerical simulation in large aspect ratio domains, at *Pr*=1 (Stevens et al., 2018). The maximum for higher modes moves towards larger wave numbers, i.e., small structures, as was shown already in fig. 6. The width of the peaks also broadens significantly in the same way.

The higher modes are not only characterised by smaller structures, but also by faster dynamics as is shown by evolution of their corresponding coefficients in time in fig. 7(b). The time coefficients of the most dominant mode is always positive as the largest structure does not change sign over the time interval of the analysis, which is expected since it is the most dominant and most stable mode. The time coefficients of higher modes, however, oscillate with increasing frequencies. The exact frequencies are shown in the temporal Fourier spectrum in fig. 7(d). There, the increase of the frequencies is shown by a shift of the maximum to the right. However, we also see that the maximum of one even and its consecutive odd mode are located at the same frequency. Furthermore, the spectra of even modes decay much quicker than the spectra of the odd modes for larger frequencies. So far we have no good explanation for this peculiar observation, which needs further investigation.

Overall, we see that the TSS can be well separated from the turbulent background by proper orthogonal decomposition and occur as the first eigenmode with a wave number $k \approx 1$ as previously reported by others for such large scale structures. The turbulent background is represented by higher order modes which also show a significant faster dynamics.

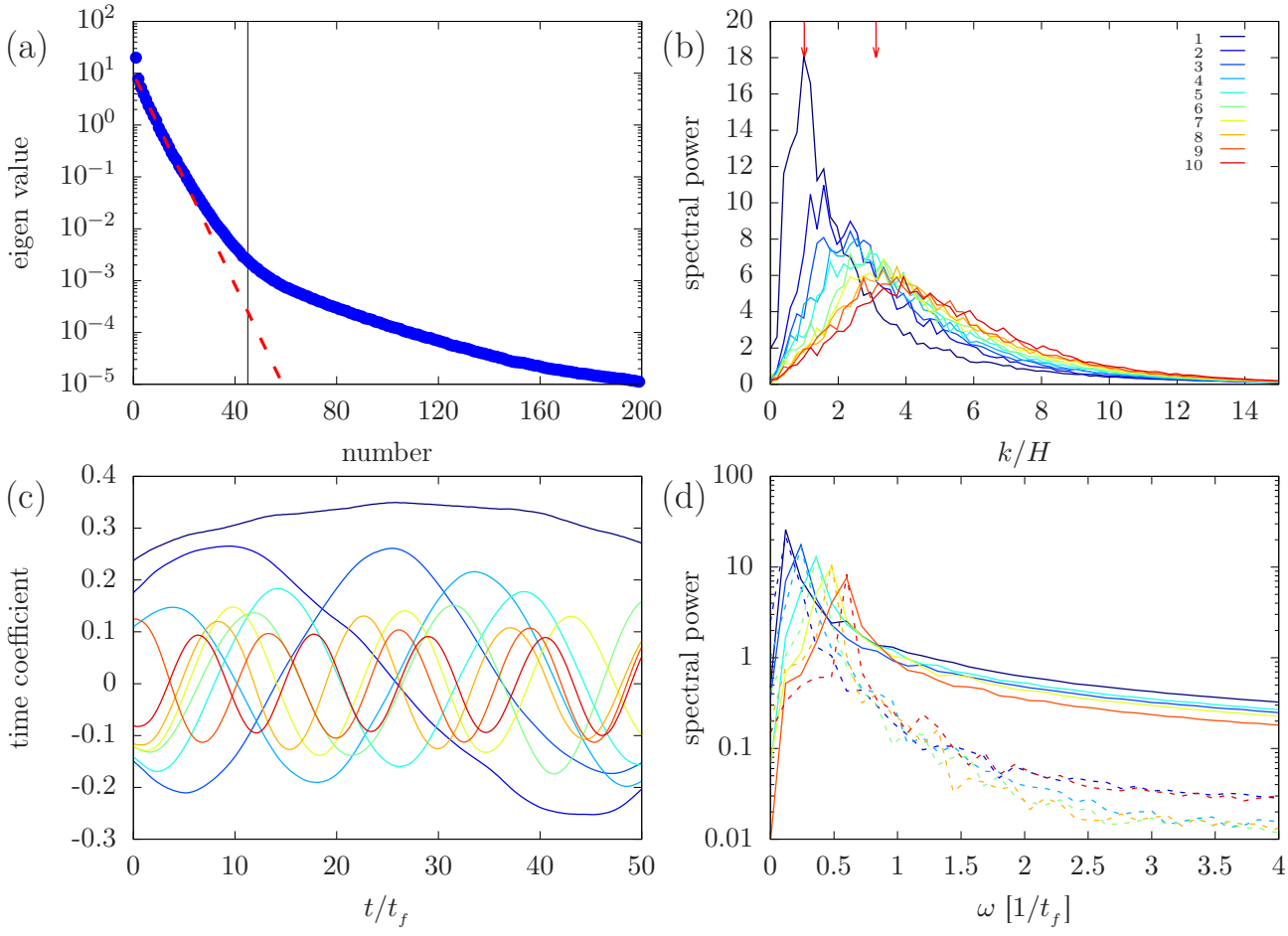

Figure 7. Properties of the POD modes shown in fig. 6. (a): Eigenvalue spectrum. The red dashed line marks and exponential decay. The black vertical line at 45 marks the mode at which the eigenvalues decay slower. Both lines are meant as guides to the eyes. (b): Spatial Fourier spectra of the first ten POD modes (color coded, see legend). The two red down-pointing arrows mark critical wave numbers for the onset of convection ($k = 3.12$) and $k = 1$ (c): Temporal evolution of the time coefficient of the first 10 POD modes. Colors as in (b). (d): Fourier transform of the time coefficients shown in (c). Line colors are as in (b and c). Odd modes are represented by solid lines, even modes by dashed lines.

4. Conclusions

We have presented spatially and temporally resolved velocity measurements of all three components of the entire flow field in Rayleigh-Bénard convection. By studying the flow in a rectangular cell with an aspect ratio between its lateral dimension and height of $\Gamma = L/H = 16$, we have investigated the shape and dynamics of the large scale turbulent super structures. The fluid was water at $T_m = 20.0^o$C, which was seeded with 50 μm large fluorescent polyethylene microspheres that were illuminated with UV light and observed by 6 CMOS cameras from different angles. The position, the velocity and the acceleration of the observed particles was calculated using the *Shake-The-Box* algorithm and the complete three-dimensional Eulerian velocity field was calculated via FlowFit.

Using these techniques we could clearly see the line pattern formed by rising plumes close to the bottom plate. Also upon temporal averaging the large scale *turbulent superstructures* (TSS) were revealed, and found to have a typical wave number of $k = 1$, as previously observed in numerical simulation (Ambrish Pandey & Schumacher, 2018; Stevens et al., 2018). We have further separated the slowly varying large scale pattern from the faster small scale pattern by using proper orthogonal decomposition of the vertical velocity field. There, the mode corresponding to the largest eigenvalue contains the turbulent superstructure. The first eigenvalue is about 1.5 times larger than the second eigenvalue and consecutive eigenvalues quickly decrease nearly exponentially for the first 40 eigenvalues.

With the setup presented here, it is possible to generate TSS and observe their evolution with 'Shake-The-Box' particle tracking in Rayleigh-Bénard cells of large aspect ratios Γ. Hence in the future, we plan to acquire and analyse more data in order to answer questions such as, whether the TSS can also be detected in Lagrangian properties, and how efficient particles located in one TSS are transported to neighboring rolls. We also want to investigate how their morphology and dynamics change with the control parameters, most importantly *Ra* and Γ. In fact, we have already successfully conducted measurements with the same setup in a $\Gamma = 8$ cell as well as for Rayleigh numbers in the range $1 \times 10^5 \lesssim Ra \lesssim 13 \times 10^6$. We will present according results in future publications.

Acknowledgements

We acknowledge extensive support with hard- and software for illumination and image acquisition by LaVision GmbH. We thank C. Fuchs, S. Risius, T. Herrmann, T. Kleindienst and J. Lemarechal for their contributions to the RBC sample and J. Agocs for his support during set-up of the experiment as well as the photographic work. This work was supported by the Deutsche Forschungsgemeinschaft (DFG) through Grant No. BO 5544/1 -1 as part of the Priority Programme on Turbulent Superstructures (DFG SPP 1881).

References

Ahlers, G., Grossmann, S., & Lohse, D. (2009). Heat transfer and large scale dynamics in turbulent Rayleigh-Bénard convection. *Rev. Mod. Phys.*, *81*, 503–538.

Ambrish Pandey, J. D. S., & Schumacher, J. (2018). Turbulent superstructures in Rayleigh-Bénard convection. *Nature Communications*, *9*, 2118.

Bénard, H. (1900). Les tourbillon cellulaire dans une nappe liquide. *Rev. Gén. Sci. pures et apll.*, *11*, 1261.

Berkooz, G., Holmes, P., & Lumley, J. L. (1993). The proper orthogonal decomposition in the analysis of turbulent flows. *Annual Review of Fluid Mechanics*, *25*(1), 539-575.

Bodenschatz, E., Pesch, W., & Ahlers, G. (2000). Recent developments in Rayleigh-Bénard convection. *Annu. Rev. Fluid Mech.*, *32*, 709-778.

Bosbach, J., Schanz, D., nd Phillip Godbersen, & Schröder, A. (2021). Spatially and temporally resolved measurements of turbulent Rayleigh-Bénard convection by Lagrangian particle tracking of long-lived helium-filled soap bubbles. In *14th international symposium on particle image velocimetry.*

Chillà, F., & Schumacher, J. (2012). New perspective in turbulent Rayleigh–Bénard convcection. *Eur. Phys. J. E*, *35*, 58.

Gesemann, S., Huhn, F., Schanz, D., & Schröder, A. (2016). From noisy particle tracks to velocity, acceleration and pressure fields using b-splines and penalties. In *18th international symposium on the application of laser and imaging techniques to fluid mechanics.*

Grossmann, S., & Lohse, D. (2000). Scaling in thermal convection: A unifying view. *J. Fluid. Mech.*, *407*, 27-56.

Hartlep, T., Tilgner, A., & Busse, F. H. (2003, Aug). Large scale structures in rayleigh-bénard convection at high rayleigh numbers. *Phys. Rev. Lett.*, *91*, 064501.

Huisman, S. G., van der Veen, R. C., Sun, C., & Lohse, D. (2014). Multiple states in highly turbulent Taylor-Couette flow. *Nature Communications*, *5*, 3820.

Ibbeken, G., Green, G., & Wilczek, M. (2019, Sep). Large-scale pattern formation in the presence of small-scale random advection. *Phys. Rev. Lett.*, *123*, 114501.

Kadanoff, L. P. (2001). Turbulent heat flow: Structures and scaling. *Phys. Today*, *54*(8), 34-39.

Krug, D., Lohse, D., & Stevens, R. J. (2020). Coherence of temperature and velocity superstructures in turbulent Rayleigh–bénard flow. *Journal of Fluid Mechanics*, *887*, A2.

Lohse, D., & Xia, K.-Q. (2010). Small-scale properties of turbulent Rayleigh-Bénard convection. *Annu. Rev. Fluid Mech.*, *42*, 335-364.

Lumley, J. L. (1967). Similarity and the turbulent energy spectrum. *Phys. Fluids*, *10*, 855.

Moller, S., Resagk, C., & Cierpka, C. (2021). Long-time experimental investigation of turbulent superstructures in Rayleigh–Bénard convection by noninvasive simultaneous measurements of temperature and velocity fields. *Experiments in Fluids*, *62*, 1-18.

Paolillo, G., Greco, C. S., Astarita, T., & Cardone, G. (2021). Experimental determination of the 3-d characteristic modes of turbulent Rayleigh–Bénard convection in a cylinder. *Journal of Fluid Mechanics*, *922*, A35.

Rayleigh, L. (1916). On convection currents in a horizontal layer of fluid, when the higher temperature is on the under side. *Philosophical Magazin*, *32*, 529.

Schanz, D., Gesemann, S., & Schröder, A. (2016). Shake-the-box: Lagrangian particle tracking at high particle image densities. *Experiments in Fluids*, *57*, 70.

Schanz, D., Gesemann, S., Schröder, A., Wieneke, B., & Novara, M. (2012, dec). Non-uniform optical transfer functions in particle imaging: calibration and application to tomographic reconstruction. *Measurement Science and Technology*, *24*(2), 024009.

Schanz, D., Novara, M., & Schröder, A. (2021). Shake-The-Box particle tracking with variable timesteps in flows with high velocity range (VT-STB). In *14th international symposium on particle image velocimetry.*

Schanz, D., Schröder, A., Gesemann, S., Michaelis, D., & Wieneke, B. (2013). Shake-The-Box: A highly efficient and accurate tomographic particle trakcing velocimetry (tomo-ptv) method using prediction of particle positions. In *10th international symposium on particle image velocimetry-piv13.*

Stevens, R. J. A. M., Blass, A., Zhu, X., Verzicco, R., & Lohse, D. (2018). Turbulent thermal superstructures in Rayleigh-Bénard convection. *Phys. Rev. Fluids*, *3*, 041501.

Wieneke, B. (2008). Volume self-calibration for 3d particle image velocimetry. *Exp. Fluids*, *45*, 549.